AAS 26-103

MANEUVER-BASED SCALE ESTIMATION IN VISUAL SLAM FOR AUTONOMOUS ASTEROID EXPLORATION

Claudio Matarrese*, Pietro Califano†, Felice Piccolo‡, and Paolo Panicucci§

Small-body exploration is increasingly constrained by saturated ground infrastructure and high mission costs. Onboard navigation based on Visual Simultaneous Localization and Mapping (SLAM) offers a promising solution by autonomously estimating both spacecraft state and small-body environment, which is largely unknown before arrival. Unfortunately, monocular visual SLAM suffers from scale ambiguity, limiting autonomy or requiring dedicated ranging sensors. This work proposes a cost-effective method that resolves scale ambiguity by leveraging proximity maneuvers within a factor graph SLAM framework, only employing standard sensors: a monocular camera, an IMU, and a star tracker. The algorithm explicitly estimates a maneuver-related scale parameter by jointly optimizing visual measurements and maneuver dynamics through a dedicated two-body dynamics factor. The scale parameter aligns measured maneuvers with the scale of the current trajectory. Upon convergence, a reset step rescales the entire solution using analytical scaling laws, enabling consistent estimation of the spacecraft state, landmark map, and gravitational parameter. Online incremental smoothing is achieved via the iSAM2 solver. A Monte Carlo analysis shows that after a few maneuvers, the algorithm reliably and robustly recovers the correct scale, yielding position errors below 20 meters and accuracy of gravity and velocity estimates within a few percent.

INTRODUCTION

Interest in small-body exploration has grown over the past two decades, yet missions still rely heavily on ground-in-the-loop navigation, demanding substantial economic and human resources. This reliance requires high data downlink and manual processing, which strain ground infrastructures as the number of concurrent missions increases. This causes scheduling conflicts and reduces operational flexibility, ultimately raising mission costs.

Monocular visual Simultaneous Localization and Mapping (SLAM) offers a promising alternative, enabling autonomous navigation and characterization capabilities while adopting sensors with low cost, weight, power, and size requirements. By applying multi-view geometry algorithms to imaged surface features, it reconstructs the spacecraft trajectory and asteroid shape, providing a basis for estimating dynamical properties with minimal dependency on ground operations and prior characterization. Akin to terrestrial applications, SLAM for small-body exploration has progressively shifted from filter-based to graph-based estimation formulations. Graph-based methods overcome the filtering-based limitations by exploiting the SLAM problem sparsity, avoiding marginalizations,

*Ph.D. Student, Dept. of Aerospace Science and Technology, Politecnico di Milano, claudio.matarrese@polimi.it

†Ph.D. Student, Dept. of Aerospace Science and Technology, Politecnico di Milano, pietro.califano@polimi.it

‡Ph.D. Graduate, Dept. of Aerospace Science and Technology, Politecnico di Milano, felice.piccolo@polimi.it

§Assistant Professor, Dept. of Aerospace Science and Technology, Politecnico di Milano, paolo.panicucci@polimi.it

and repeatedly relinearizing,[1,2] yielding more accurate and stable solutions with superior efficiency. This work adopts a factor-graph formulation solved incrementally (i.e., efficiently updating the solution as new measurements arrive) using iSAM2.[3]

Several recent works adopt iSAM2 (or its predecessor) as the optimization backbone for SLAM-based proximity navigation, and demonstrate that monocular vision, coupled with sufficiently informative dynamical models, can support the estimation of both relative motion and target physical properties. Tweddle et al.[4] introduced a factor-graph framework that remarkably integrates relative translational and rotational dynamics into a factor graph framework, estimating target center of mass, principal axes, and inertia ratios. Building on similar principles, Takeishi et al.[5] jointly estimated the relative pose, shape, and physical parameters of an asteroid, separately modeling the absolute dynamics of inspector spacecraft and asteroid by relying on onboard IMU measurements. Dor et al.[6] proposed a complete SLAM system that incorporates orbital motion constraints through kinematic and dynamic factors, enabling joint estimation of spacecraft states and asteroid parameters without relying on inertial measurements.

However, the fundamental scale ambiguity inherent to monocular imaging is typically left unresolved or addressed through strong assumptions. In fact, from monocular images alone, it is impossible to determine the true scale of the observed body and the relative trajectory. In particular, among the asteroid navigation works, either the absolute scale is assumed or not recovered[5–7] or Deep Space Network (DSN) measurements are used,[8] contradicting the emerging paradigm of spacecraft autonomy. Conversely, exploration missions such as Hayabusa2,[9] OSIRIS-Rex,[10] and Hera[11] rely on range sensors or LiDARs, particularly heavy and power-intensive; moreover, the sensor combination necessitates complex image–LiDAR registration, an intensive process traditionally carried out on the ground.[12] This ultimately brings the navigation loop back to the same operational limitations SLAM initially aimed to overcome.

Takahashi and Scheeres[13,14] introduce a breakthrough technique named ΔV ranging. The core idea is to exploit spacecraft maneuvers to resolve monocular scale ambiguity, leveraging the discrepancy between the observed and predicted parallax after a maneuver. If the scale (i.e., the spacecraft distance) is incorrect, the observed parallax will differ from the one predicted by the dynamical model. By comparing these two sources of information, the estimator can resolve the scale thus estimate the asteroid's size and gravity. This approach is particularly advantageous for small-body missions, which feature frequent correction maneuvers performed with minimal propellant expense. Their more recent work[14] applies the methodology to complete operational settings involving inertial hovering and closed orbits. However, it employs simplified optical measurements (i.e., line-of-sight direction and body's angular size) and assumes a spherical asteroid. Therefore, the integration of realistic optical observables and ΔV ranging in a full SLAM framework for arbitrary asteroid shapes remains an open research point.

This paper specifically tailors ΔV ranging within a SLAM framework. The proposed system jointly estimates the spacecraft-body relative state, a sparse pointwise map of the target's surface, and the gravitational parameter, effectively overcoming visual scale ambiguity through the incorporation of maneuver information. Only hardware with a high-performance-to-cost ratio is employed: a monocular camera, an inertial measurement unit, and a star tracker, avoiding reliance on costly laser-based active sensors and extensive ground-based navigation support. The state-of-the-art SLAM back-end employs a factor graph formulation integrating visual measurements with a model of relative dynamics.
The core technique adopted consists in explicitly and efficiently estimating a global scaling parame-

ter in correspondence of maneuvers, through a novel scale-determination factor based on two-body dynamics. The procedure is enabled by coherent scaling relationships among the problem unknowns that describe how each quantity transforms when the overall scene scale is changed, while respecting visual parallax and two-body dynamics. Two operational modes alternate in the proposed pipeline. The *scale mode* processes new maneuvers using the aforementioned factor, concurrently optimizing the scale parameter and all other state variables. Upon scale convergence, a *reset step* enforces the new scale across the entire state set through the scaling relations, in contrast with previous implementations of ΔV ranging[13,14] where state magnitudes were implicitly adjusted by the estimator. Afterward, in *base mode* the algorithm conventionally propagates two-body dynamics with maneuver ΔVs, naturally providing a correctly scaled solution.

PROBLEM STATEMENT

SLAM Navigation Problem

Fig. 1 depicts reference frames and notable world points used throughout the work. Considering an asteroid in heliocentric orbit, the frame I coincides with ECLIPJ2000 and has its origin in the asteroid center of mass A. Neglecting the minimal asteroid motion along its orbit, I and A approximately inertially-fixed. The frame A is barycentric and aligned with the principal axes of the asteroid. The spacecraft frame S is barycentrical and spacecraft-fixed and, as depicted in Fig. 1, its x-axis coincides with the camera's boresight axis $\hat{z}_C$. The camera frame C is also barycentrical.

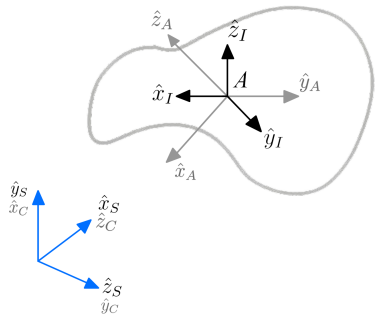

Figure 1: Representation of reference frames used throughout the work.

The scenario considered in this paper involves a spacecraft orbiting an asteroid within its sphere of influence, where the asteroid's gravity field, coupled with other perturbing effects, governs the spacecraft's trajectory. The spacecraft performs predefined proximity maneuvers to modify its relative trajectory, enhancing asteroid surface coverage and aiding the scale estimation process. The asteroid is assumed non-rotating, aligning the asteroid-fixed frame A with the inertial frame I. While unrealistic, this assumption does not affect the validity of the proposed navigation formulation and serves to simplify the relative dynamics. Incorporating rotational kinematics would not alter the scale estimation methodology, being independent of scale.

The measurements used in the navigation solution are outlined below, along with their roles in the proposed methodology and the corresponding error models. The associated noise distributions are used by the estimator to define factor covariances that encode uncertainty in the factor graph.

- *2D feature points* $\tilde{\mathbf{y}}_{f,i}$ extracted from images correspond to the projections of landmarks L_f, and are the primary input for the SLAM back-end to estimate both the spacecraft's relative

motion and the asteroid map. Landmarks are distinctive regions on the asteroid's surface identified by the visual front-end and matched across views. Adopting the pinhole camera model, the ideal projection of a surface landmark L_f onto the image plane at time t_i in homogeneous coordinates is:[6,15]

$$ {}^{h}\mathbf{y}_{f,i} = K\, T_{CI}(t_i)\, {}^{h}\mathbf{r}^{I}_{L_f A} \tag{1} $$

Feature extraction error is modeled with additive zero-mean Gaussian noise with covariance $\Sigma_{\text{proj}} = \sigma^2_{\text{proj}} I_{2\times 2}$.

- *Star tracker measurements* of the spacecraft's inertial attitude R_{IS} are used only during maneuvers to map measured velocity changes from frame S to frame I. Although the non-rotating asteroid assumption implies $R_{AS} = R_{IS}$, the unrealistic convenience of using star tracker data to fully determine the relative attitude is prevented. Noise is added as $\tilde{R}_{IS} = R_{IS} \exp\left([\boldsymbol{\nu}_R]^{\wedge}\right)$, where the 3D vector $\boldsymbol{\nu}_R$ has zero-mean and covariance $\Sigma_R = \sigma^2_R I_{3\times 3}$.

- *Direct prior measurements* of the spacecraft's relative attitude R_{AS}, position $\mathbf{r}^I_{SA}$, and velocity $\mathbf{v}^I_{SA}$ are provided at the initial time $t = t_0$, as commonly done in spacecraft graph-based SLAM.[4–6] These initial values may originate from a previous navigation phase or from ground-based measurements. Anchoring the first pose is essential during the initial visual SLAM phase with high uncertainty in the dynamics, while the initial velocity is needed to initialize and propagate the spacecraft state. Prior measurements are modeled by adding zero-mean Gaussian noise to ground truth values, following the standard definition of a prior factor in factor-graph-based estimation.[16]

- *Maneuver measurements* are modeled as impulsive velocity changes derived from integrated onboard accelerometer data, yielding the discrete increment $\Delta\tilde{\mathbf{v}}^S$ in the spacecraft frame and its timestamp τ. While no error is attributed to τ, maneuver noise is modeled by additive Gaussian error $\boldsymbol{\epsilon}_{\Delta v} \sim N(0, \sigma^2_{\Delta v} I_{3\times 3})$, which depends from accelerometer noise spectral density σ_{aH} and maneuver duration ΔT as $\sigma_{\Delta v} = \sigma_{aH}\Delta T$.[14] To match the estimator's dynamical model, the measurement $\Delta\tilde{\mathbf{v}}^S$ must be transformed to the inertial frame I using the star tracker measurement $\tilde{R}_{IS}$, yielding the following noise model:

$$ \Delta\tilde{\mathbf{v}}^I = \exp\left([\boldsymbol{\nu}_R]^{\wedge}\right)\left(\Delta\mathbf{v}^I + \boldsymbol{\epsilon}_{\Delta v}\right) \tag{2} $$

The proposed methodology incrementally estimates the set of unknown variables X using a maximum a posteriori (MAP) formulation. The state includes the relative spacecraft poses T_{IS} (or equivalently T_{AS}), inertial velocities $\mathbf{v}^I_{SA}$, the asteroid gravitational parameter μ_a, and the positions of surface landmarks $\mathbf{r}^I_{L_f A}$, which are assumed fixed. State updates sequentially process measurements, without marginalizations, and are performed at selected keyframes to limit redundant visual information. The estimator combines landmark observations with two-body relative dynamics and impulsive maneuvers. A central objective is the recovery of a consistent metric scale across the reconstructed environment, spacecraft trajectory, and gravity field; this is achieved by leveraging the coupling between visual measurements and maneuver-induced odometry through the explicit optimization of a scale parameter during scale-estimation mode.

Scale Ambiguity and its Resolution

With only monocular observations, it is fundamentally impossible to recover the similarity transformation between the reconstructed scene and the true environment.[15] As a result, both the ref-

erence frame and the scale in pure monocular SLAM are arbitrary. To fix frame and scale, low-covariance prior distributions on the first camera poses are often used.

Introducing a motion model (e.g., two-body dynamics) constraining consecutive spacecraft states could resolve the scale of the SLAM solution, provided sufficient accuracy. In practice, poor initial knowledge of velocity and gravity hinders this method of resolving scale ambiguity. Since gravity depends on the relative distance, the estimation of the small body's gravitational parameter μ_a is also subject to scaling indeterminacy. Without any absolute scale information, two-body dynamics alone cannot resolve the scale ambiguity: they are affected by it, making gravity estimation is inherently linked to scale recovery. In general, breaking scale ambiguity requires non-visual metric data with low uncertainty, such as ranging, maneuver measurements, a known μ_a, or precise state priors. Accurate and valid scale recovery depends on all metric information being consistent with the true scale within high-probability bounds.

In the proposed framework, spacecraft maneuvers are leveraged to resolve scale ambiguity and enable gravity estimation. It is worth recalling that only central gravity must be estimated, as higher order spherical harmonics are scale invariant. The key insight is that the spacecraft's thrust is independent of the relative distance, yet it directly affects relative translational dynamics. When paired with visual line-of-sight measurements, the known thrust produces an absolute displacement that effectively acts as a ranging observation. In general, any known absolute force part of a dynamical model, when combined with parallax data between camera poses, can provide absolute scale information. In essence, the proposed algorithm starts from a monocular SLAM solution where scale is initially anchored by highly uncertain priors, unlike conventional methods. As maneuvers are incorporated, the algorithm shall converge to the true scale of the trajectory, surface map, and gravitational parameter, thereby resolving the initial ambiguity.

METHODOLOGY

Graph-Based Visual SLAM

The graph-based SLAM back-end (i.e., the estimator) solves the MAP estimation problem that seeks the state X^* maximizing the posterior $p(X|Z)$:[17]

$$X^* = \arg\max_X p(X|Z) = \arg\max_X p(X) \prod_{i=1}^{m} p(z_i|X_j) = \arg\min_X \sum_{i=0}^{m} \|h_i(X_j) - z_i\|^2_{\Sigma_i} \quad (3)$$

$p(X|Z)$ is factorized into priors $p(X)$ and measurement likelihoods $p(z_i|X_j)$, as each measurement $z_i \in Z$ only depends on variables $X_j \in X$ and is assumed to be independent from other measurements. Assuming Gaussian noise, the likelihoods are defined by the residual $h_i(X_j) - z_i$ and its covariance Σ_i, h_i being a (generally nonlinear) measurement function. In this way, MAP becomes a nonlinear least squares problem.
Factor graphs visually represent the problem by connecting factor nodes, which portray measurement likelihoods or priors, to variable nodes X_j, with edges indicating dependency.[18] Factor graphs effectively represent problems, like SLAM, where each measurement depends on a small and localized subset of all variables. iSAM2[3] leverages this property to incrementally solve the least squares problem in Eq. 3, updating only affected variables while maintaining batch-level accuracy.

The visual SLAM system processes feature points from a front-end module to estimate spacecraft poses and surface landmarks. The corresponding factor graph includes two factor types: pose priors and projection factors, as shown as an example in Fig. 2. Prior factors are constructed given mean

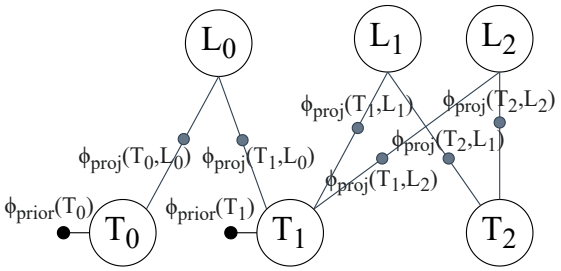

Figure 2: Basic SLAM factor graph. Factors are represented as filled color-coded dots, while variables are represented as white circles.

estimates and covariances for the first two poses. Projection factors link a keyframe poses and a landmarks penalizing the reprojection error between the measured one $\tilde{\mathbf{y}}_{f,k}$ and the predicted one $\mathbf{y}_{f,k}$,[16] computed with the pinhole camera model in Eq. 1. In pure monocular SLAM, priors on the first two poses resolve similarity ambiguity by fixing frame and scale. Alternatively, a relative pose constraint between the first two keyframes suffices. The implementations of prior and projection factors and the iSAM2 solver are given in the GTSAM library *. This basic SLAM graph will be augmented with two-body dynamics factors.

A simple keyframe-based visual SLAM pipeline is adopted, which is sufficient for the controlled simulation environment with regular parallax and no outliers. An evenly spaced subset of images is selected as keyframes, which are the only images taking part in the optimization. Keyframe spacing is doubled around impulsive maneuvers to enhance parallax for scale estimation, consistently with the state-of-the-art practice of introducing cutoff times. Landmarks are introduced in the state once they are observed in at least three keyframes to ensure reliable triangulation. As soon as this condition is verified, a landmark is initialized and inserted in the graph with projection factors to be optimized for the first time.
Overall, each keyframe update consists of feature classification, pose and landmark initialization, factor insertion, and an incremental iSAM2 optimization, as illustrated in the Visual SLAM blue box in Fig. 5. The spacecraft pose is initialized using correspondences with reconstructed landmarks via a PnP solution,[19] refined next by Bundle Adjustment Motion (i.e., keeping landmarks fixed). New landmarks are triangulated from three views. Both pose and landmark initializations preserve the current scale: poses inherit scale from the map, and landmarks inherit it from camera poses. Scale consistency is maintained throughout the optimization by co-visible landmark constraints.

Scaling Relations

To estimate an explicit scale parameter based on ΔV ranging, relations are derived to characterize how the problem unknowns transform under isotropic geometric scaling of the scene. The relations respect two-body dynamics and visual line-of-sight geometry, linking spacecraft velocity, impulsive maneuvers, and the asteroid gravitational parameter between two solutions whose trajectories and surface landmarks differ only by a global scale factor.

Let s be a scaling factor, with primed variables indicating scaled quantities. Scaling the scene

*https://gtsam.org/

means scaling the camera position profile (and the map points) by s:

$$\mathbf{r}'^{I}_{SA}(t) = s\mathbf{r}^{I}_{SA}(t) \tag{4}$$

Preserving multi-view geometry under scaling means leaving the angles between observation rays unchanged. To satisfy this condition, and assuming a rotating asteroid for generality, the angular velocity of the Local-Vertical-Local-Horizontal (LVLH) spacecraft frame relative to the asteroid-fixed frame must be invariant under scaling. Since the asteroid's rotation rate is unaffected by geometric scaling, this requirement implies that the inertial angular velocity of the spacecraft LVLH frame remains unchanged (equally, the evolution of the true anomaly). As a result, geometric scaling does not alter the time parametrization of the problem. Therefore, as the position vector must sweep the same angle over the same time interval but at a different radial distance, the velocity scales linearly:

$$\mathbf{v}'^{I}_{SA}(t) = s\mathbf{v}^{I}_{SA}(t) \tag{5}$$

Due to the linearity of the time derivative and the invariance of the time scale, the acceleration scales linearly as well; for the two-body acceleration, this leads to:

$$\mu'_a = s^3\mu_a \tag{6}$$

By the same argument, the velocity change follows linear scaling as well, preserving the shape of the trajectory:

$$\Delta\mathbf{v}'^{I} = s\Delta\mathbf{v}^{I} \tag{7}$$

The derived relations underpin the proposed scale estimation method. First, Eq. 7 shows that a correcting scale factor can be indirectly recovered by estimating the maneuver intensity consistent with the current trajectory, defining the scale-determination factor presented hereafter. Moreover, once a scale reliable estimate is available, the equations enable a coherent rescaling of the entire solution through the *reset step*.

Two-body Dynamics and Maneuver Odometry

Building on the visual SLAM foundation, two-body and maneuver dynamics are inserted through a custom factor, whe Two-Body Problem (TBP) factor, that evaluates nonlinear integration errors. The Two-Body Problem with Scale (TBP,S) factor extends it by introducing the maneuver scale parameter $s_{\Delta V}$, which scales the maneuver contribution to match the solution's current scale. This enables effective ΔV ranging, estimating a global scale parameter with a localized optimization, respecting and taking advantage of the locality structure of factor graphs.

Two-Body Problem Factor The TBP factor ϕ_{TBP} expresses the position and velocity integration error, propagating the continuous-time dynamics with the current estimate of the asteroid's gravitational parameter μ_a and the maneuver data. This factor follows the formulation of Tweddle et al.[4] and Califano et al.,[20] adopting a nonlinear dynamic model with state noise compensation.

The continuous-time dynamical model is:

$$\begin{cases} \dot{\mathbf{r}}^{I}_{SA}(t) = \mathbf{v}^{I}_{SA}(t) \\ \dot{\mathbf{v}}^{I}_{SA}(t) = -\dfrac{\mu_a}{r^3_{SA}(t)}\mathbf{r}^{I}_{SA}(t) + \Delta\tilde{\mathbf{v}}^{I}\delta(t-\tau) + \mathbf{w}_v(t) \end{cases} \tag{8}$$

where $\mathbf{w}_v$ is a 3-dimensional zero-mean Gaussian white noise with power spectral density $Q_{\mathrm{TBP}} = \sigma^2_{\mathrm{TBP}} I_{3\times3}$, and aims to represent unmodeled perturbations (e.g., third-body, SRP).

The TBP factor is defined by the factor error $\mathbf{e}_{k,k+1}$ and its associated covariance $\Lambda(t_{k+1})$. The error $\mathbf{e}_{k,k+1}$ is the deviation between the position and velocity in X at t_{k+1}, and the prediction obtained by full nonlinear integration of the dynamics in Eq. 8 from t_k.[4] The associated factor covariance $\Lambda(t_{k+1})$ is propagated from a zero initial condition with the continuous-time Lyapunov equation.[4] Covariance propagation across the maneuver (from the instant right before τ^- to the one right after τ^+) is performed as follows, in between the nonlinear integration:

$$\Lambda(\tau^+) = \Lambda(\tau^-) + \begin{bmatrix} 0_{3\times3} & 0_{3\times3} & 0_{3\times1} \\ 0_{3\times3} & \sigma^2_{\Delta v} I_{3\times3} + \sigma^2_R [\Delta\tilde{\mathbf{v}}]^\wedge [\Delta\tilde{\mathbf{v}}]^\wedge & 0_{3\times1} \\ 0_{1\times3} & 0_{1\times3} & 0 \end{bmatrix} \tag{9}$$

Intuitively, the velocity covariance incorporates accelerometer and attitude measurement uncertainties. This result is obtained using the discretized Lyapunov equation with piecewise-constant white noise,[21] and by noting that the state transition matrix across the maneuver is the identity.[14] Finally, it is remarked that the presence of the gravitational parameter does not directly influence covariance propagation due to the structure of the Lyapunov equation and the Jacobian of the dynamics, and because it is a constant noise-free parameter. The factor covariance reflects intrinsic modeling uncertainty,[4] while the uncertainty in μ_a is handled globally by iSAM2 as part of the state rather than within individual odometry factors, analogously to batch estimators. The same principle applies to any unknown but constant parameter in the dynamics.

Two-Body Problem Factor with Maneuver Scale. For eased convergence and accuracy, an explicit scale parameter is optimized in correspondence of maneuver events. However, explicitly estimating the unknown metric scale by attaching a single scale state to every pose and landmark would create a densely connected graph, demanding expensive batch optimization over all variables. To preserve sparsity, the TBP,S factor $\phi_{\mathrm{TBP,S}}$ is introduced, exploiting the distance-dependent coupling between dynamics and multi-view geometry to find a localized scale parameter that still has global validity. Rather than adjusting the trajectory to match the absolute scale implied by the maneuvers, the proposed formulation fixes the current visual trajectory as a reference and fits the scale so that the predicted maneuvers align with it, in accordance with Eq. 7. This approach localizes the scale variable around each maneuver, enabling efficient updates.

The scale parameter associated with the maneuvers $s_{\Delta V}$ is included in the state, and multiplies the maneuver contribution in the dynamics of Eq. 8:

$$\begin{cases} \dot{\mathbf{r}}^I_{SA}(t) = \mathbf{v}^I_{SA}(t) \\ \dot{\mathbf{v}}^I_{SA}(t) = -\dfrac{\mu_a}{r^3_{SA}(t)}\mathbf{r}(t) + s_{\Delta V}\Delta\tilde{\mathbf{v}}\delta(t-\tau) + \mathbf{w}_{v,S} \end{cases} \tag{10}$$

The process noise $\mathbf{w}_{v,S}$ has density $Q_{\mathrm{TBP,S}} = \sigma^2_{\mathrm{TBP,S}} I_{3\times3}$. The factor error and its associated covariance are propagated with the same procedure of the TBP factor. However, since the $\Delta\mathbf{v}$ contribution is multiplied by the scale factor $s_{\Delta V}$, the covariance across the maneuver is updated as:

$$\Lambda(\tau^+) = \Lambda(\tau^-) + s^2_{\Delta V} \begin{bmatrix} 0_{3\times3} & 0_{3\times3} & 0_{3\times2} \\ 0_{3\times3} & \sigma^2_{\Delta v} I_{3\times3} + \sigma^2_R [\Delta\tilde{\mathbf{v}}]^\wedge [\Delta\tilde{\mathbf{v}}]^\wedge & 0_{3\times2} \\ 0_{2\times3} & 0_{2\times3} & 0_{2\times2} \end{bmatrix} \tag{11}$$

As with the gravitational parameter in the TBP factor, the scale parameter $s_{\Delta V}$ does not affect the covariance propagation in any other way.

Algorithm Outline

The methodology revolves around the TBP,S factor, which is inserted into the graph for localized scale estimation at each maneuver event, defining the system's operation in *scale mode*. Once the scale parameter $s_{\Delta V}$ converges, a *reset step* applies the scaling relations to consistently update all estimated variables with the new scale. The processing of a maneuver ends as the system transitions to *base mode*, where the standard TBP factor propagates the impulsive velocity change, and the maneuver-related scale parameter is removed. This cycle repeats for each maneuver.

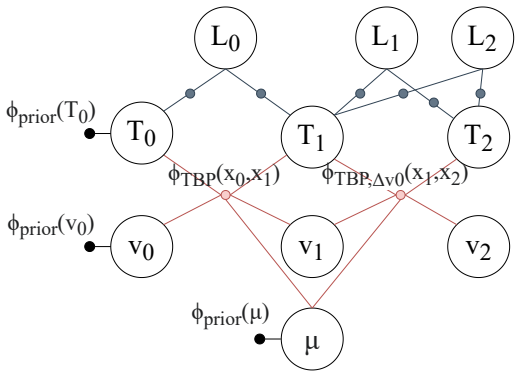

Figure 3: SLAM factor graph with two-body dynamics odometry and asteroid gravitational parameter. Note the factor between variables at $k = 1$ and $k = 2$ containing the first maneuver $\Delta\mathbf{v}_0$.

Base Mode Formulation The base mode factor graph, shown in Fig. 3, extends the visual SLAM structure (Fig. 2) by adding TBP factors between keyframes (accounting for maneuvers when present) and introducing the asteroid's gravitational parameter and relative spacecraft velocities as unknowns. Prior factors are assigned to the initial velocity and the gravitational parameter; the latter weakly constrains μ_a during early optimization stages, when its observability is limited. The second keyframe prior is omitted since the scale is anchored by spacecraft dynamics.
This graph-based formulation mirrors the filter-based problem in Takahashi and Scheeres,[14] with the exclusion of maneuver magnitude and execution time estimation. Within this framework, the optimization can converge to the true scale, provided that the prior distributions include the true values within high-probability regions. However, unlike scale mode, this formulation treats scale implicitly: only states adjacent to the maneuver are directly influenced, while the rest adjust indirectly through odometry. As iSAM2 favors the update of recent variables over global refinement, scale convergence is hindered, making base mode ineffective for scale estimation. This motivates the scale mode formulation for explicit estimation of the global scale parameter $s_{\Delta V}$.

Scale Mode Formulation The scale mode formulation incorporates the TBP,S factor for spacecraft states between the maneuvers within the current processing window, introducing the maneuver-related scale parameter $s_{\Delta V}$ in the corresponding factor graph (Fig. 4), enabling tightly coupled scale estimation. All TBP,S factors share the same scale variable $s_{\Delta V}$, reflecting that all maneuvers

relate to the absolute scale. iSAM2 updates the solution at each keyframe as in base mode. Although scale is a global property, this formulation enables its localized estimation from recent maneuvers alone. As $s_{\Delta V}$ scales maneuvers to fit the current trajectory, the corresponding global scale factor for the solution is:

$$s = 1/s_{\Delta V} \tag{12}$$

This formulation assumes the trajectory and map maintain their scale during optimization. However, an additional scaling degree of freedom is introduced, associated with the maneuver-related parameter $s_{\Delta V}$. In the absence of scale-fixing constraints, the problem admits a family of equivalent solutions in which the trajectory is isotropically rescaled while $s_{\Delta V}$ varies inversely, yielding internally consistent but non-unique minima. To prevent undesired global rescaling during scale mode, scale-fixing constraints are introduced through priors: when scale mode is activated, the initial pose, velocity, and gravitational parameter priors are replaced by the current solution marginals, preserving the existing trajectory scale within their uncertainty bounds. This strategy is most effective once marginal covariances have sufficiently contracted.
Despite the formal scale ambiguity, iSAM2 tends to absorb ΔV scale information into $s_{\Delta V}$, since its incremental updates preferentially adjust newly introduced variables, leaving the global trajectory scale largely unaffected as long as $s_{\Delta V}$ is linked only to recent maneuvers. However, due to the dense connectivity induced by the global variable μ_a linked to every TBP factor, scale-fixing constraints remain necessary.

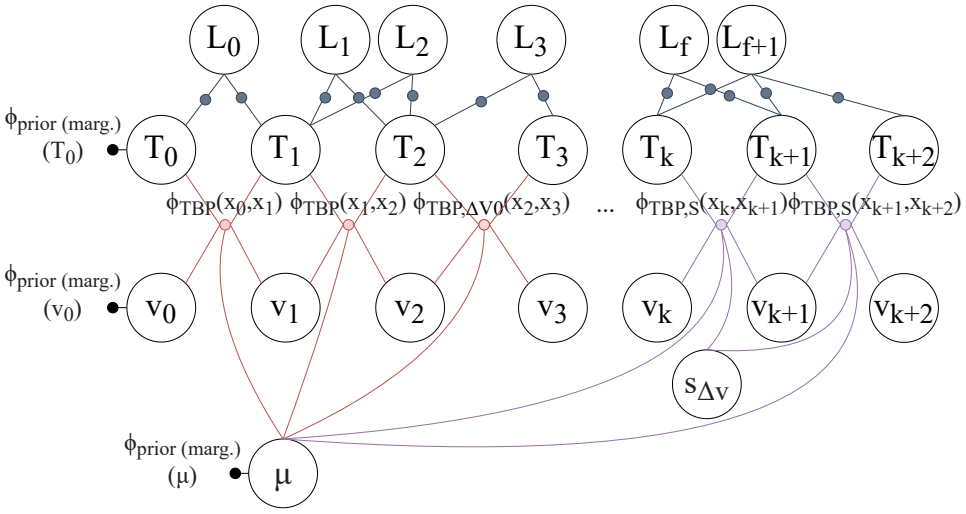

Figure 4: Generic factor graph for *scale mode*, including the scale parameter $s_{\Delta V}$. New maneuvers (between keyframes k and k+1, k+1 and k+2) are processed with the TBP,S factor while old ones (keyframes 2-3) are represented by the TBP factor.

The overall navigation algorithm is presented in Fig. 5. After the initialization of the starting map and the second pose projection and TBP factors are added for each new pose and velocity, calling iSAM2 before the loop repeats. When the first maneuver is reached, the algorithm enters *scale mode*, inserting the factor $\phi_{\mathrm{TBP,S}}$ for the new ΔV and swapping the initial prior factors for the first pose, velocity, and gravitational parameter with the corresponding values marginalized from the current estimates. The navigation proceeds refining new states and $s_{\Delta V}$. If a new maneuver is encountered while still in scale mode, the corresponding TBP,S factor is added. To leave scale

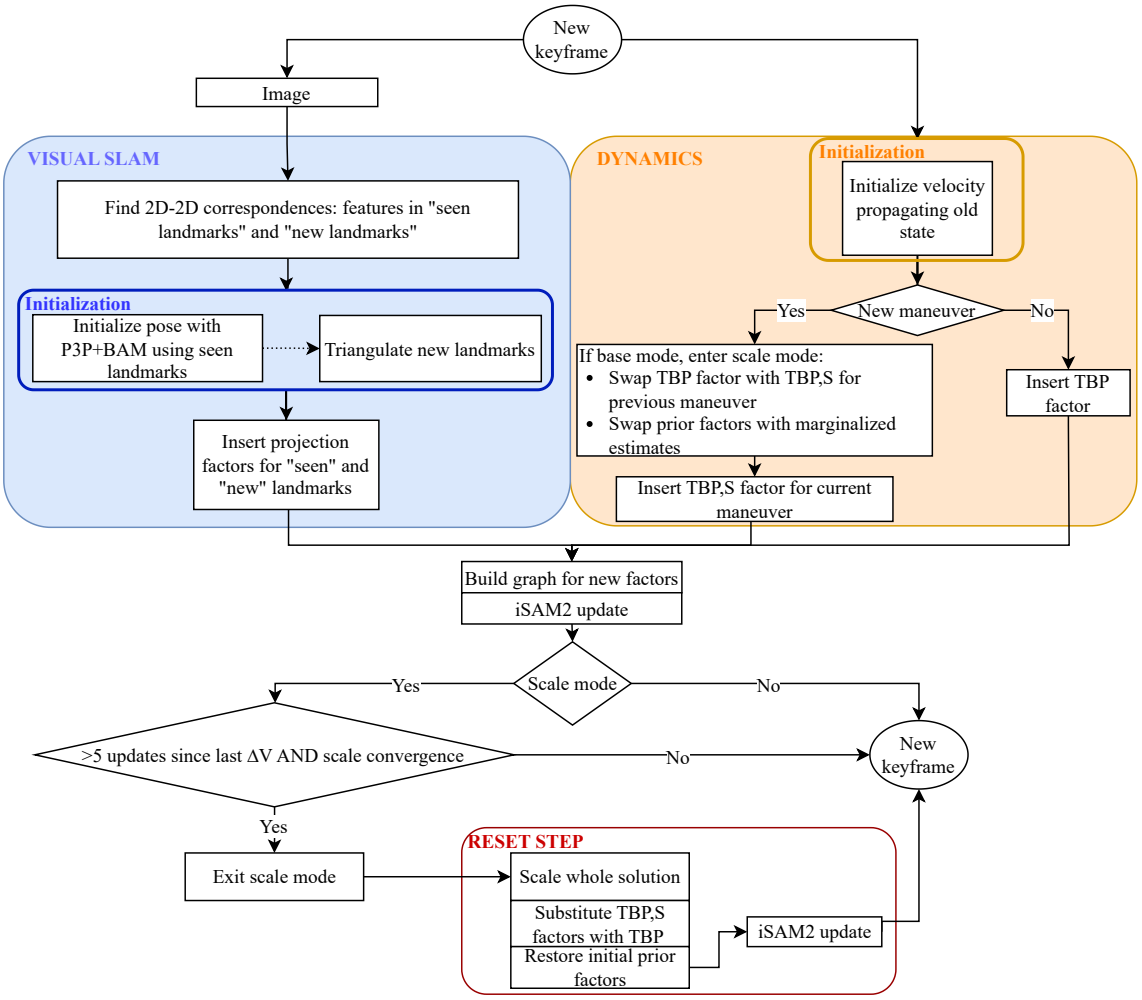

Figure 5: Flowchart of a full loop of the navigation algorithm.

mode, two criteria must be satisfied: at least 5 keyframes must have been processed after the last maneuver, and the scale parameter's estimate must have settled within a 2% threshold over the last three updates. This tuning prevents the simultaneous processing of an excessive number of maneuvers, which would densely connect the problem favoring the fall into the scale indeterminacy family. As scale mode is terminated, the *reset step* is performed: the estimate of $s_{\Delta V}$ is used to scale the whole set of unknowns using the scaling relations. The scaled variables are immediately optimized by iSAM2 as the algorithm transitions back to base mode, removing scale-fixing constraints by restoring prior factors to their original values. Each new maneuver triggers scale mode. To improve observability, TBP,S factors are always applied to the two most recent maneuvers, with earlier ones modeled by TBP factors, as shown in Fig. 4.

Before the first maneuver is processed, a geometrically consistent initialization for the second keyframe pose and map is required to provide a stable starting point for subsequent optimization and scale estimation. As the second keyframe directly affects landmark scaling and subsequent PnP-based pose estimates, its initialization must preserve the scale implied by the initial pose prior, minimizing the error correction performed by iSAM2. The procedure, outlined in Algorithm 1,

initializes pose and map via a two-view reconstruction, scaled using the spacecraft–asteroid distance from the first pose prior under the assumption that the landmark centroid approximates the asteroid's center of mass. Accuracy can vary with asteroid's shape and camera placement.

Algorithm 1 Scale-preserving initialization

Require: First two keyframes, first pose prior $\tilde{T}_{IS_0}$
Ensure: Correctly scaled second pose T_{IS_1} and landmarks
1: Extract 2D–2D feature correspondences between the first and second keyframes.
2: Compute essential matrix E from these correspondences using 8-point algorithm.
3: Recover relative pose (R, t). ▷ Normalize $\|t\| = 1$ so that the baseline has unitary length.
4: Triangulate landmarks in the reference frame of the first keyframe. ▷ The two keyframes and landmarks compose the *unscaled scene*, where the first keyframe is the origin.
5: Select landmarks whose projections lie on the convex hull of features in the first keyframe.
6: Compute the centroid C (mean position) of the selected landmarks.
7: Let d_C be the distance from C to the first pose (origin) in the unscaled scene.
8: Compute scale factor $s_{\text{init}} = r_{S_0A}/d_C$, where r_{S_0A} is the prior spacecraft–asteroid distance.
9: Scale poses and landmarks of the unscaled scene with s_{init}. ▷ The first pose stays the identity.
10: Roto-translate poses and landmarks with $\tilde{T}_{IS_0}$, aligning the first keyframe with the prior $\tilde{T}_{IS_0}$.
11: **return** The scaled second pose T_{IS_1} and the scaled landmarks.

RESULTS

To evaluate the behavior, performance, and robustness of the proposed navigation solution, two analyses are performed: a Monte Carlo simulation tests robustness and consistency, while a parametric analysis studies the influence of the accelerometer noise σ_{aH}.

Simulation Setup

Table 1: Parameters for spacecraft dynamics.

Parameter	Symbol	Value
Asteroid gravitational parameter	μ_a	$2.36\ \mathrm{m}^3/\mathrm{s}^2$
Asteroid-Sun distance	r_{AO}	1.62 AU
Spacecraft surface reflectivity	ρ_s	0.4
Spacecraft area	A_s	$0.4\ \mathrm{m}^2$
Spacecraft mass	m_s	24 kg
SRP noise spectral density	σ_{SRP}	$2 \times 10^{-9}\ \mathrm{m/s^2}/\sqrt{\mathrm{Hz}}$

The proposed navigation algorithm is evaluated in a numerical simulation environment, which generates all non-visual measurements using the same models implemented in the estimator. Spacecraft translational dynamics are propagated in the inertial frame under asteroid's spherical gravity, third-body solar perturbations, solar radiation pressure (SRP), and impulsive maneuvers. SRP is modeled using a cannonball formulation with additive white noise to model secondary effects. Higher-order gravity harmonics are neglected for simplicity, being inherently scale-invariant. Parameter values are reported in Table 1. Spacecraft attitude is assumed to maintain constant nadir pointing toward the asteroid, ensuring continuous camera visibility. The simulated target is the near-Earth asteroid 25143 Itokawa. Landmarks are selected evenly on its surface and treated as inertially

fixed points. At each image acquisition, visible landmarks are projected onto the image plane using a pinhole camera model, excluding occluded points. Image resolution and camera focal length are selected respectively as 1024×1024 pixels and 900 pixels to ensure adequate asteroid coverage in the image frame. A statistical front-end simulation emulates KLT feature tracking[22] and loop closure, producing realistic but outlier-free image measurements. This approach simplifies the test environment and isolates back-end performance from visual front-end failures, but it is still capable of simulating feature tracking loss and non-Gaussian noise. Simulation parameters and image capture rate (288 images per revolution) are tuned to match the dataset of Morrell et al.[23]

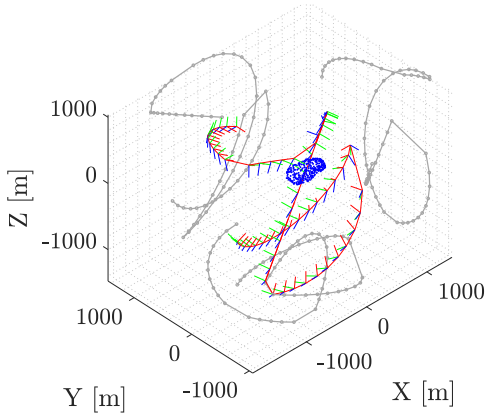

Figure 6: Ground truth keyframes of the spacecraft trajectory shown in the inertial frame I. The spacecraft's attitude is represented by red ($\hat{\mathbf{x}}_S$), green ($\hat{\mathbf{y}}_S$), and blue ($\hat{\mathbf{z}}_S$) axes, while landmarks are depicted as blue dots.

Table 2: Numerical values used to generate simulated measurements, with relative uncertainty for priors.

Parameter	**Value**	**Relative uncertainty**
Attitude prior std. dev.	180 arcsec	-
Radial position prior std. dev.	150 m	12.5%
Position prior in other directions std. dev.	50 m	4.2%
Velocity prior std. dev.	5×10^{-3} m/s	10%
Accelerometer noise σ_{aH}	10^{-5} m/s$^2/\sqrt{\text{Hz}}$	-
Maneuver duration T	20 s	-
Star tracker std. dev. σ_R	30 arcsec	-
Grav. parameter prior	10 m^3/s^2	-
Grav. parameter prior std. dev.	10 m^3/s^2	-

Ground-truth keyframes are shown in Fig.6. The trajectory maintains distances of about 1 km and features four impulsive maneuvers. The chosen flight path is dominated by the asteroid's gravity, maintains low eccentricity, and provides broad surface coverage. Coupled with strong maneuvers, this setup enhances scale observability. Keyframes are selected at 1.1 h intervals (approximately one in five images), with maneuvers placed midway. Keyframe spacing is further increased around the final maneuver, based on numerical testing. TBP,S noise $\sigma^2_{\text{TBP,S}}$ is set to 10^{-13} m^2/s^4/Hz to improve scale convergence, while higher TBP noise $\sigma^2_{\text{TBP}} = 8 \times 10^{-11}$ m^2/s^4/Hz accounts for the unmodeled SRP forces, to yield realistic uncertainty estimates. The projection factor stan-

dard deviation σ_{proj} is tuned to 1 px. Table 2 summarizes the measurement parameters. To test scale reconstruction performance, large uncertainties are assigned to radial position and velocity priors, intentionally introducing initial scale errors, while transversal position components are more tightly constrained. The loose gravitational parameter prior provides only a weak early constraint. Accelerometer noise is lower than typical commercial IMUs ($\sigma_{aH} > 10^{-4}$ m/s$^2/\sqrt{\text{Hz}}$), due to the importance of maneuver measurements, but significantly higher than state-of-the-art sensors ($\sigma_{aH} < 10^{-8}$ m/s$^2/\sqrt{\text{Hz}}$).[14]

Monte Carlo Analysis

A Monte Carlo simulation of 300 runs is conducted by randomly varying the stochastic simulation parameters within their prescribed uncertainties (Table 2). During scale mode, estimates and the corresponding covariances are transformed using the scaling relations, taking into account the covariance of $s_{\Delta V}$. For clarity, errors are brought to the spacecraft LVLH frame $(\mathbf{r}, \boldsymbol{\theta}, \mathbf{h})$.

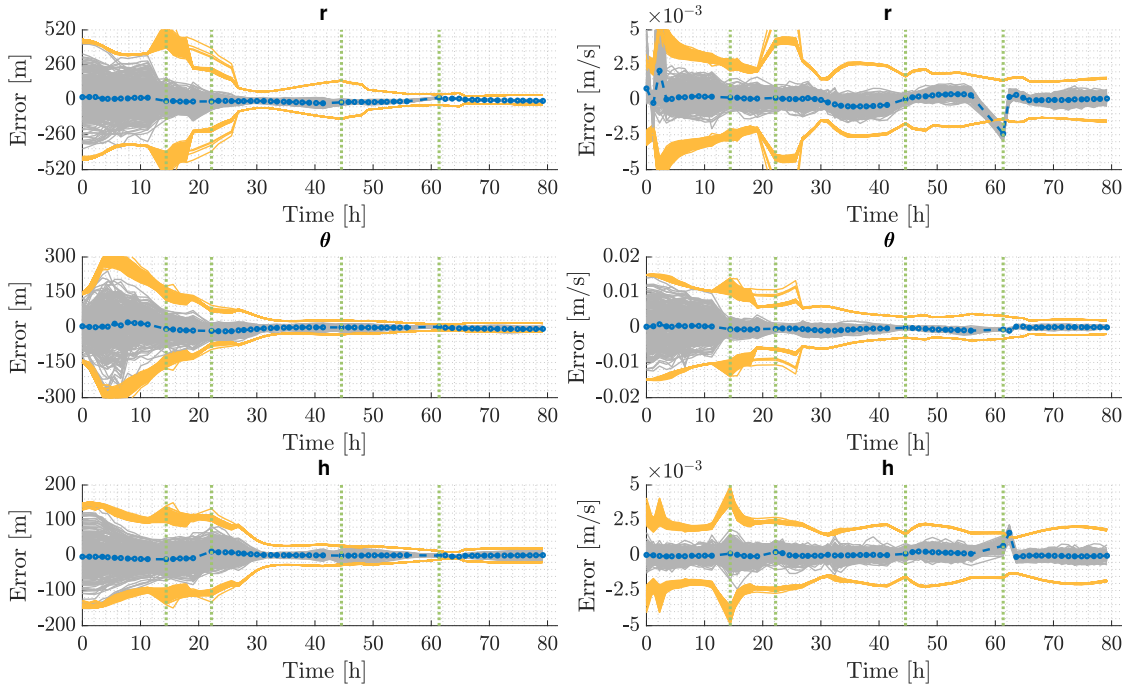

(a) Position (b) Velocity

Figure 7: Instantaneous absolute position and velocity errors (gray) in the LVLH frame for the Monte Carlo. Orange lines depict 3-sigma bounds; the blue dashed line is the ensemble mean of all errors. Green vertical lines mark the start of scale mode.

Figure 7 shows the instantaneous errors and 3-sigma bounds for all runs. Those refer to the sequential error of each position-velocity pair at the moment it is first added and optimized, mimicking a filter-like behavior. Initial variability, due to differences in prior generation, is consistently reduced after processing maneuvers, confirming the effectiveness of ΔV ranging. Before the first maneuver, the error on the prior (mostly radial) propagates to subsequent states. After the second maneuver, the radial position error is significantly reduced; however, subsequent maneuvers are es-

sential for refining the estimates and further decreasing uncertainty. Similar behavior is observed in the along-track velocities, which are the dominant component and the one most affected by scale variations. Intuitively, all sigma bounds show a significant decrease in correspondence of reset steps. In some cases, weaker scale convergence delayed the reset step, nevertheless causing no impact on final estimates.
Similarly, Fig. 8 shows the evolution of gravitational parameter error. On average, the high prior bias is quickly reduced as the gravitational parameter is fit to the trajectory's scale, but dispersed offsets still remain before the first maneuvers. After the insertion of the first ΔV, the scale parameter becomes observable, strongly reducing the error on the gravitational parameter.

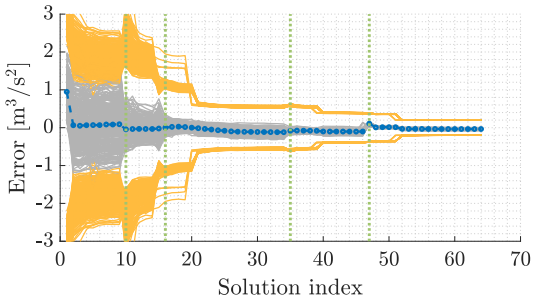

Figure 8: Evolution of absolute errors (gray) and 3-sigma (orange) in the gravitational parameter for each Monte Carlo run.

All 3-sigma bounds are characterized by a slight rise when entering scale mode, a behavior that stems from scale indeterminacy in scale mode. When marginal covariances used as new priors remain large, $s_{\Delta V}$ inherits high variance, which propagates to state estimates. Later, with better scale estimates, the marginalized priors constrain the scale more effectively, yielding tighter estimates of $s_{\Delta V}$. More effective scale-fixing methods would likely reduce the scale parameter's variance.

The final position and velocity errors are shown in Fig. 9, demonstrating accurate scale recovery, with position errors under 20 m and velocity relative errors between 0.5% and 2%, as well as representative uncertainties. These results confirm the algorithm's ability to recover from large initial errors, particularly in scale, by leveraging odometry and maneuver knowledge. The final error distribution indicates that maneuvers enable recovery of the full similarity transformation between the estimate and the ground truth. This is attributed to the inertial-frame formulation with a fixed asteroid, whereby ΔV ranging implicitly constrains also the translational component. This property may not extend to rotating asteroids, where additional degrees of freedom arise.
The ensemble mean of position errors oscillates around zero, confirming accurate scale estimation. The undulating trend is attributed to SRP effects that vary with the spacecraft's trajectory. This also explains the consistent underestimation of the gravitational parameter, with a median relative error across runs of 1.5%. Including the SRP into the dynamical model is a key direction for future work. The spacecraft's attitude error departs from the precise prior reaching maximum errors around 0.6 deg, as the relative attitude is only constrained by projection factors thus dominated by feature drift.

Figure 10 shows the ensemble mean of the map's Hausdorff distances, where Hausdorff errors per landmark are mapped onto the ground truth 3D model. Reconstruction quality varies among surface portions that are more or less observed by the spacecraft. Errors remain below 3 m in well-observed regions, confirming accurate scale estimation, and suggesting that feature noise is the dominant source of map uncertainty.

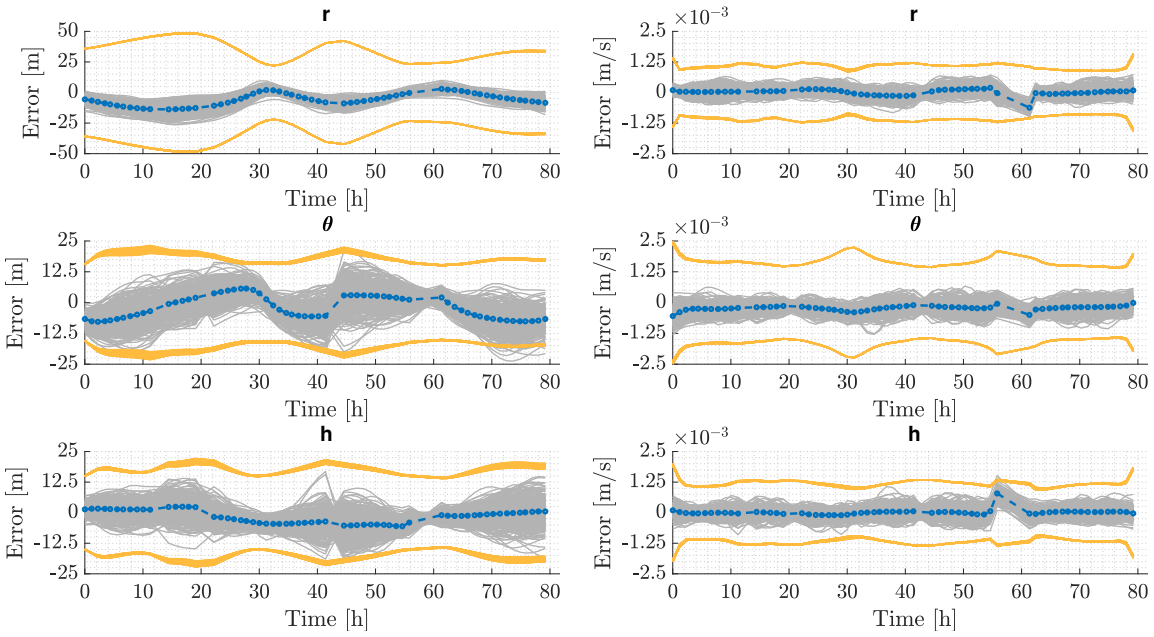

(a) Position (b) Velocity

Figure 9: Absolute errors (gray) and 3-sigma bounds (orange) in LVLH for the final solution of each run of the Monte Carlo. The blue dashed line is the ensemble average across runs.

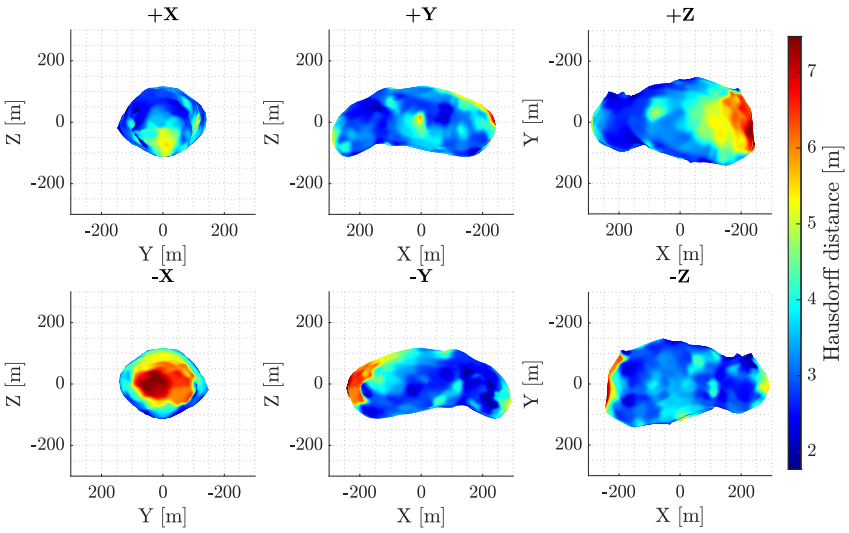

Figure 10: Ensemble average across Monte Carlo runs of landmark Hausdorff distances.

Accelerometer Noise Parametric Analysis

This final analysis examines how accelerometer noise affects navigation and scale estimation accuracy. A covariance parametric study is conducted using four logarithmically-spaced noise levels (Table 3). Above the upper bound ΔV measurements lose informativeness and may cause failure, while the lower bound avoids exploring a regime of diminishing returns.

Table 3: Accelerometer noise values for the parametric analysis. The relative uncertainty is computed with respect to the weakest maneuver (the first).

σ_{aH} [m/s^2/$\sqrt{\text{Hz}}$]	$\sigma_{\Delta V}$ $[m/s]$	**Relative uncertainty**
10^{-3}	4.5×10^{-3}	20%
4×10^{-4}	1.8×10^{-3}	8%
10^{-4}	4.5×10^{-4}	2%
5×10^{-5}	2.2×10^{-4}	1%

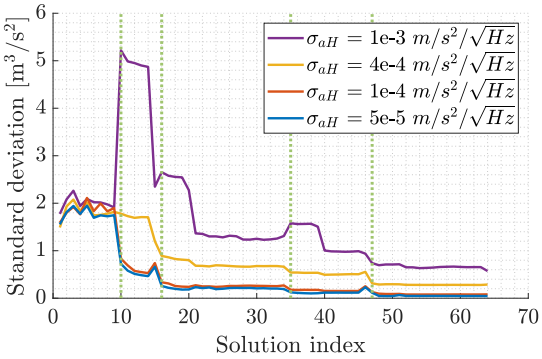

Figure 11: Ensemble 3-sigma of the Monte Carlo error profiles of the gravitational parameters for different values of σ_{aH}. Green vertical lines mark the start of scale mode.

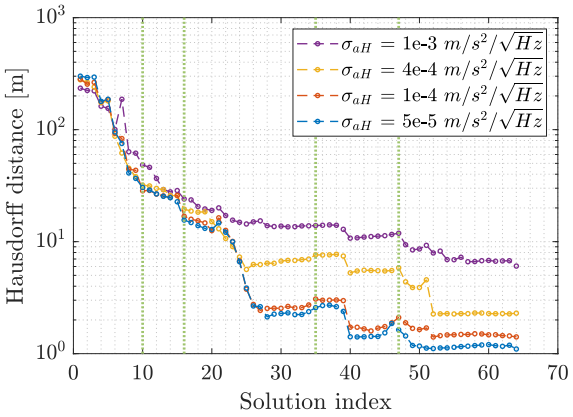

Figure 12: Ensemble 3-sigma across Monte Carlo runs of the mean landmark Hausdorff distance for different values of σ_{aH}. Green vertical lines mark the start of scale mode.

Fig. 11 shows the ensemble 3-sigma bounds across Monte Carlo runs of the gravitational parameter. As gravity is highly sensitive to scale errors, there is a marked gap between the three highest values of σ_{aH}. Higher noise leads to larger early deviations that require more steps to compensate for the errors in the ΔV measurements; particularly poor results are observed with the highest accelerometer noise. Conversely, diminishing returns in error dispersion are observed between the two lowest noise levels, as the uncertainty in the other measurements dominates. Fig. 12 confirms the effect of scale uncertainty on map reconstruction. The 3-sigma ensemble bounds clearly grow with noise, reflecting degraded shape reconstruction. At high noise levels, the benefit of scale reset

diminishes, whereas noticeable differences between the two lowest noise values highlight the map's sensitivity to small changes in scale accuracy.

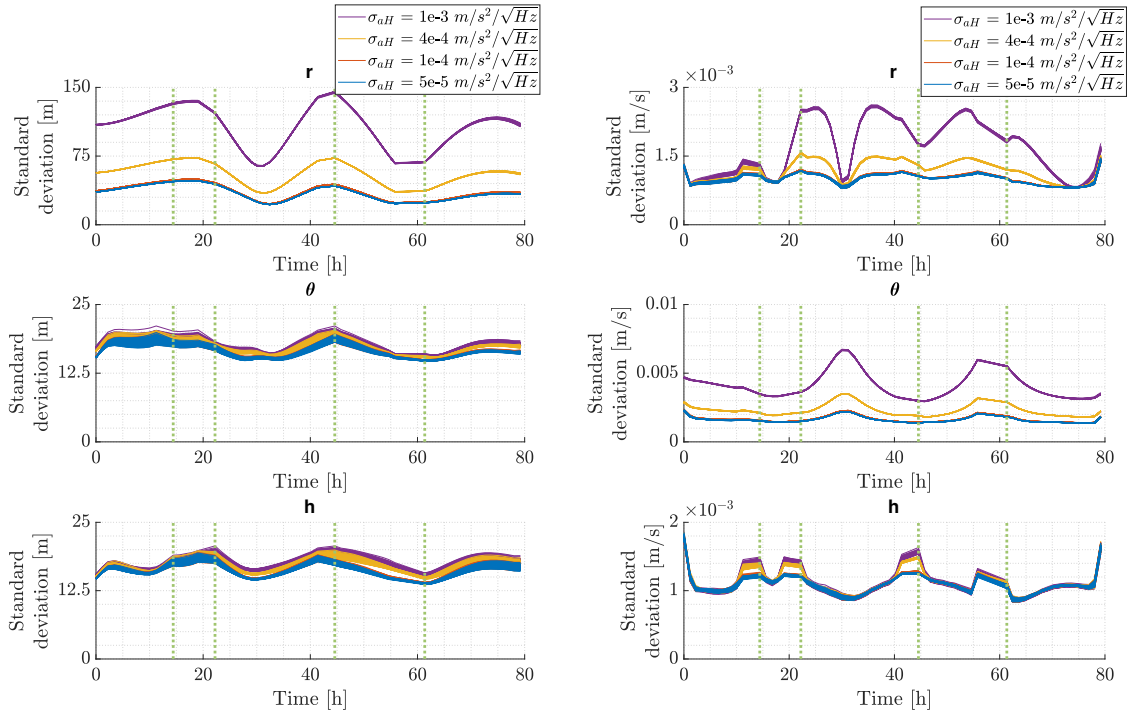

(a) Position (b) Velocity

Figure 13: 3-sigma bounds in LVLH of the final positions and velocities of Monte Carlo runs for different values of σ_{aH}. Green vertical lines mark the keyframe times right before maneuvers.

The final position and velocity standard deviations in Fig. 13 confirm that high maneuver noise primarily degrades scale observability, as shown by radial position and along-track velocity. These components are the most sensible to leftover scale errors, and specifically, to errors in the gravitational parameter. In truth, relative dynamics in general is affected, as the dispersion for other velocity components increases after maneuver events for higher accelerometer noise. At lower noise levels, instead, diminishing returns are again observed.
The final gravitational parameter error distribution in Fig. 14 shows great dependency on σ_{aH}, valuing the most precise ΔV measurements and highlighting the sensitivity of μ_a to scale estimation.

In summary, when $\sigma_{aH} > 4 \times 10^{-4}$ $\mathrm{m/s^2/\sqrt{Hz}}$, dynamics estimation (i.e., velocities, gravity) becomes unreliable and scale errors propagate into position, map, and μ in particular. Satisfactory performance is achieved with $\sigma_{aH} = 10^{-4}$ $\mathrm{m/s^2/\sqrt{Hz}}$, below which returns diminish. Nevertheless, the lowest noise level further improves gravity and map reconstruction. For effective scale estimation, maneuver measurements should maintain relative uncertainty below 1% (1-sigma).

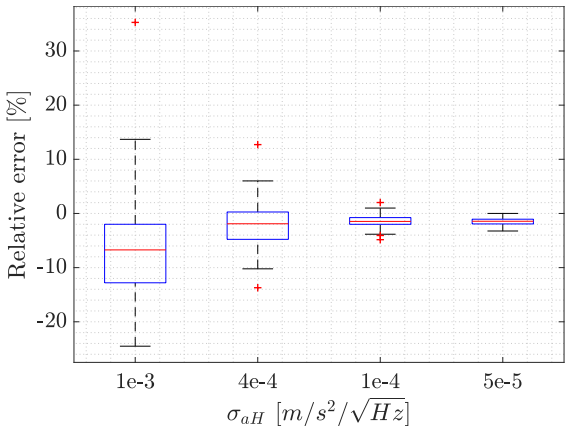

Figure 14: Box plots of Monte Carlo distributions of gravitational parameter final relative errors for different values of σ_{aH}.

CONCLUSIONS

This work presents a method to resolve scale ambiguity in monocular SLAM around small bodies by exploiting proximity maneuvers, using only cost-effective onboard sensors and no laser instruments or ground support. Impulsive maneuvers are integrated into a factor-graph framework, where visual and two-body dynamical constraints are jointly optimized to estimate spacecraft states, a surface map, and the gravitational parameter. As a novel contribution, scale is recovered by optimizing a localized maneuver-related scaling parameter that aligns the measured maneuvers with the current, potentially mis-scaled solution. The coupling between visual measurements and maneuver-induced dynamics renders the metric scale observable: in presence of scale errors, the parallax inferred from images becomes inconsistent with that predicted by the dynamical model when an absolute driving force is known. Upon parameter convergence, the recovered scale is coherently propagated to the full solution via analytical scaling relations.

Simulation results demonstrate robust and accurate scale recovery after multiple maneuvers, with final position errors below 20 m, map errors below 10 m, and velocity and gravitational parameter errors within a few percent, despite large prior uncertainty. Maneuver measurement accuracy around 1-2% is proven to be paramount for precise scale reconstruction, to which gravitational parameter estimation is particularly sensitive.

NOTATION

Reference frames and points in $\mathbb{R}^3$ are denoted with capital Latin letters. A translation vector between points X, Y $\in \mathbb{R}^3$ is $\mathbf{r}^O_{YX} := (Y - X)$, with coordinates in frame O. Unitary vectors are denoted with the hat symbol $\hat{\mathbf{v}}$, and the Euclidean norm as $v = |\mathbf{v}|$. The rotation matrix $R_{AB} \in$ SO(3) denotes the transformation from frame B to frame A such that $\mathbf{v}^A = R_{AB}\mathbf{v}^B$. Finally, a pose transformation $T_{AB} \in$ SE(3) is:

$$T_{AB} := \begin{bmatrix} R_{AB} & \mathbf{r}^A_{BA} \\ 0_{1\times 3} & 1 \end{bmatrix}$$

For Lie group and Lie algebra elements, the exponential map and logarithm map are denoted with the classical notation $\exp(\cdot)$ and $\log(\cdot)$.[6,24] For n-vectors $\mathbf{v}$, the symbol $[\cdot]^\wedge$ denotes the hat operator,

mapping $\mathbf{v}$ to an element in the Lie algebra; the inverse vee operator is instead $[\cdot]^\vee$.

REFERENCES

[1] F. Dellaert and M. Kaess, "Square Root SAM: Simultaneous Localization and Mapping via Square Root Information Smoothing," *The International Journal of Robotics Research*, Vol. 25, No. 12, 2006, pp. 1181–1203.

[2] M. Kaess, A. Ranganathan, and F. Dellaert, "iSAM: Incremental Smoothing and Mapping," *IEEE Transactions on Robotics*, Vol. 24, No. 6, 2008, pp. 1365–1378.

[3] M. Kaess, H. Johannsson, R. Roberts, V. Ila, J. J. Leonard, and F. Dellaert, "iSAM2: Incremental smoothing and mapping using the Bayes tree," *The International Journal of Robotics Research*, Vol. 31, No. 2, 2012, pp. 216–235.

[4] B. E. Tweddle, A. Saenz-Otero, J. J. Leonard, and D. W. Miller, "Factor Graph Modeling of Rigid-body Dynamics for Localization, Mapping, and Parameter Estimation of a Spinning Object in Space," *Journal of Field Robotics*, Vol. 32, No. 6, 2015, pp. 897–933.

[5] N. Takeishi and T. Yairi, "Visual Monocular Localization, Mapping, and Motion Estimation of a Rotating Small Celestial Body," *Journal of Robotics and Mechatronics*, Vol. 29, No. 5, 2017, pp. 856–863.

[6] M. Dor, T. Driver, K. Getzandanner, and P. Tsiotras, "AstroSLAM: Autonomous monocular navigation in the vicinity of a celestial small body—Theory and experiments," *The International Journal of Robotics Research*, Vol. 43, No. 11, 2024, pp. 1770–1808.

[7] M. Delpech, V. Bissonnette, and L. Rastel, "Vision-based navigation for proximity operations around asteroid 99942 Apophis," *Proceedings of 25th International Symposium on Space Flight Dynamics*, 2015, pp. 19–25.

[8] F. Baldini, A. Harvard, S. J. Chung, I. Nesnas, and S. Bhaskaran, "Autonomous small body mapping and spacecraft navigation," *Proceedings of the 69th International Astronautical Congress (IAC)*, 2018.

[9] S.-i. Watanabe, Y. Tsuda, M. Yoshikawa, S. Tanaka, T. Saiki, and S. Nakazawa, "Hayabusa2 mission overview," *Space Science Reviews*, Vol. 208, 2017, pp. 3–16.

[10] D. Lauretta, S. Balram-Knutson, E. Beshore, W. Boynton, C. Drouet d'Aubigny, D. DellaGiustina, H. Enos, D. Golish, C. Hergenrother, E. Howell, *et al.*, "OSIRIS-REx: sample return from asteroid (101955) Bennu," *Space Science Reviews*, Vol. 212, 2017, pp. 925–984.

[11] P. Michel *et al.*, "The ESA Hera Mission: Detailed Characterization of the DART Impact Outcome and of the Binary Asteroid (65803) Didymos," *The Planetary Science Journal*, Vol. 3, No. 7, 2022, p. 160.

[12] J. M. Leonard, J. L. Geeraert, B. R. Page, A. S. French, B. W. Ashman, P. G. Antreasian, C. Adam, E. Lessac-Chenen, L. McCarthy, D. Nelson, J. Pelgrift, E. Sahr, A. Liounis, E. Palmer, J. R. Weirich, B. M. Kennedy, N. Mastrodemos, J. Bellerose, D. Lubey, B. Rush, D. Velez, M. C. Moreau, O. Barnouin, and D. S. Lauretta, "OSIRIS-REx shape model performance during the navigation campaign," *Proceedings of the 43rd Annual AAS Guidance and Control Conference, Breckenridge, CO*, 2020.

[13] Y. Takahashi and D. J. Scheeres, "Small-Body Postrendezvous Characterization via Slow Hyperbolic Flybys," *Journal of Guidance, Control, and Dynamics*, Vol. 34, No. 6, 2011, pp. 1815–1827.

[14] S. Takahashi and D. J. Scheeres, "Autonomous exploration of a small near-earth asteroid," *Journal of Guidance, Control, and Dynamics*, Vol. 44, No. 4, 2021, pp. 701–718.

[15] R. Hartley and A. Zisserman, *Multiple view geometry in computer vision*. Cambridge university press, 2003.

[16] F. Dellaert and M. Kaess, "Factor Graphs for Robot Perception," *Foundations and Trends in Robotics*, Vol. 6, No. 1-2, 2017, pp. 1–139.

[17] C. Cadena, L. Carlone, H. Carrillo, Y. Latif, D. Scaramuzza, J. Neira, I. Reid, and J. J. Leonard, "Past, Present, and Future of Simultaneous Localization and Mapping: Toward the Robust-Perception Age," *IEEE Transactions on Robotics*, Vol. 32, No. 6, 2016, pp. 1309–1332.

[18] F. Dellaert, "Factor Graphs: Exploiting Structure in Robotics," *Annual Review of Control, Robotics, and Autonomous Systems*, Vol. 4, No. Volume 4, 2021, 2021, pp. 141–166.

[19] X.-S. Gao, X.-R. Hou, J. Tang, and H.-F. Cheng, "Complete solution classification for the perspective-three-point problem," *IEEE Transactions on Pattern Analysis and Machine Intelligence*, Vol. 25, No. 8, 2003, pp. 930–943.

[20] P. Califano, F. Piccolo, P. Panicucci, and F. Topputo, "Enhanced Full Visual Slam for Close Proximity Exploration of Asteroids Combining Incremental Smoothing with Filtering Techniques," *Proceedings of the 35th AAS/AIAA Space Flight Mechanics Meeting*, 2025, pp. 1–22.

[21] B. Schutz, B. Tapley, and G. H. Born, *Statistical orbit determination*. Elsevier, 2004.

[22] C. Tomasi and T. Kanade, "Detection and tracking of point features," *International Journal of Computer Vision*, Vol. 9, No. 137-154, 1991, p. 3.

[23] B. J. Morrell, J. Villa, S. Bandyopadhyay, D. Lubey, B. Hockman, S. Bhaskaran, D. Bayard, and I. Nesnas, "Autonomous Feature Tracking for Autonomous Approach to a Small Body," *Proceedings of ASCEND*, 2020.

[24] J. Solà, "Quaternion kinematics for the error-state Kalman filter," 2017.